

Mars Small-Spacecraft Human Exploration Resource Prospector with Aero-braking (SHERPA): Demonstrating an End-to-End Mission to Phobos Distant Retrograde Orbit

Jaime Esper¹, Buzz Aldrin²

¹NASA Goddard Space Flight Center, Greenbelt MD, USA – Jaime.Esper@nasa.gov

²Chairman, Human Space Flight Institute, Space Port Houston, TX – Buzz@hsi.buzz

Abstract

This paper summarizes an end-to-end mission design concept exploring the feasibility of using small satellites together with aero-capture technology to achieve Mars orbit insertion, and subsequent injection into a Phobos-stabilized (or distant retrograde) orbit. The science and mission objectives are to carry out a survey of the mineralogy and morphology of Phobos, to answer basic questions concerning its origin and formation, to test the cohesiveness of Phobos regolith, and to search for potential landing sites for future human or robotic spacecraft. The Mars Small-Spacecraft Human Exploration Resource Prospector with Aero-braking (SHERPA) spacecraft is based on a combination flight-tested prototype vehicle and instruments, and first principle sizing of consumables. The resulting system is fitted with an inflatable aerodynamic decelerator to effect aero-capture into a Mars elliptical orbit, on its way to achieving Phobos orbit. A computational fluid dynamics tool is used to analyze the flow-field and identify potential hot spots during aerodynamic flight. This work advocates for the use of small satellites to test out technologies and operational concepts used in sustained human exploration of Mars, and to carry out scientific exploration of the Mars system. Consistent with a systems engineering approach, this work combines elements of the NASA Human Exploration and Operations Mission Directorate, the Space Technology Mission Directorate, and the Science Mission Directorate, and proposes a scenario for science acquisition, technology verification, trajectory validation, and in-situ resource exploration. We believe these type of missions are essential forerunners to human crewed missions to Mars.

1. Introduction

Phobos has been the interest of scientific research in connection with the debate about its composition, origin, and relevance to the understanding of the early history of Mars. In 2013 one of this paper's authors (Dr. Buzz Aldrin) published a book outlining a plan for humans to colonize Mars by the year 2035 ^[1]. In it, the importance of Phobos within the context of a sustained (long term) human presence at Mars is highlighted by "allowing astronauts to tele-operate the systems that piece together the infrastructure necessary to sustain human habitation on the planet." It is this dual-interest of logistical human base and scientific research that motivates the work presented here. Small satellites and miniaturized technologies can now make scientific human precursor missions to Phobos even more relevant within the confines of cost-effective approaches to planetary exploration and technology verification.

A Phobos mission can be realized by taking full advantage of ongoing technology developments in miniaturization of spacecraft and instruments, and in development of technologies geared toward the human exploration of Mars. One family of vehicles using miniaturization and industry standards that are widely

recognized today as a powerful technology-prototyping tool are the so-called CubeSats, standardized "form-factor" spacecraft with agreed-upon interface definitions. A related approach was described in the Modular, Adaptive, Reconfigurable Systems (MARS) architecture ^[2], aiming at developing reconfigurable modular spacecraft supporting applications to a host of missions. The MARS architecture was used in designing and building a vehicle prototype flown in a suborbital demonstration in 2011, called the Small Rocket/Spacecraft Technology (SMART) Platform ^[3]. In this work, we select the SMART platform as the basis for the Small-Spacecraft Human Exploration Resource Prospector with Aero-braking (SHERPA) spacecraft bus design, since it provides more robust capabilities and options than a typical CubeSat. Nonetheless, an equivalent CubeSat-sized vehicle could very well replace the SMART-based platform, or at the very least, common-base subsystem or components can be interchanged if a compromise on performance can be traded off. The SMART bus is a micro-satellite-class platform < 100 kg in mass, compatible with the Evolved Expendable Launch Vehicle (EELV) Secondary Payload Adapter (ESPA). With flights every 2 years, secondary payloads of opportunity are ideal for reaching Mars.

2. Study Objectives

This study presents an end-to-end mission design as a contextual stage for demonstrating *feasibility* of using *small satellites* together with *aero-capture* to achieve Mars orbit insertion, and subsequent injection into a Phobos-stabilized (or distant retrograde) orbit for scientific exploration. We centered on LaRC's Hypersonic Inflatable Aerodynamic Decelerator (HIAD) as the primary aero-capture technology to deliver the vehicle to Phobos orbit, where SHERPA's two imaging cameras would carry out a detailed multi-spectral and visual survey of Phobos mineralogy and morphology. Since the objective is to demonstrate concept feasibility, we use simple minimum-energy Hohmann transfer trajectories throughout the study.

From a NASA Science Mission Directorate (SMD) perspective, *the study of Phobos presents in itself a valuable objective* insofar as it *attempts to resolve the debate concerning its composition (and likely origins)* and its relevance in understanding the early history of Mars [4]. From a NASA Human Exploration and Operations (HEO) Mission Directorate perspective, *this paper brings attention to the use of Phobos as a logistics and possible resource stage-point for the human exploration of Mars, but not as a necessary step to a Mars landed mission.* From a Space Technology Mission Directorate (STMD) perspective, *the use of aero-capture technology to achieve orbit insertion about another planet has never been tried before*, and small satellites present the ideal platform for this demonstration.

3. Why Phobos?

Based on the proposed architecture outlined in Aldrin and David, a number of studies were carried out exploring the benefits of using Phobos as a staging point for a human Mars landed mission, its use for in-situ resource utilization, and for tele-robotic and logistic operations. From a fuel perspective, using Phobos as a staging point represents little advantage as compared to a mission landing from an intermediate Mars orbit [5]. However, advantages result from logistic and operational perspectives, if radiation protection, resource utilization, low-latency teleoperation, and other pragmatic sustaining activities are considered [1, 6]. Entering a Phobos-stabilized (or distant retrograde - DRO) orbit from a High-Mars Orbit (HMO) was a common operational scenario, and is what is also used in this study.

Origin of Phobos and Connection to Human Exploration of Mars

A reference science investigation includes answering several questions related to Phobos [6, 7]: What is its composition? What is its origin? Is Phobos related to Mars? How has Phobos evolved over time? What is its internal structure? What regolith processes occur? How did the grooves form? And related to human exploitation: Is there enough hydrogen content to provide in situ resources? Is there water ice? What are the mechanical properties of the moons' surface?

One of the most likely theories on the origin of Phobos is that it is a captured D-type asteroid typical of the outer main belt, or a Trojan [7]. Figure 1 illustrates the distribution of asteroids, with the main asteroid belt lying between the orbits of Mars and Jupiter, and the Trojans and Greeks trailing and leading Jupiter, respectively. Asteroid spectral types are assigned based on their emission spectrum, color, and albedo. D-type asteroids have very low albedo, reddish spectrum, and steep visible-near infrared spectral slopes. More importantly for human exploration, they have a composition of organic-rich silicates, carbon and anhydrous silicates, and possibly water ice. The presence of ice below Phobos' regolith has not been ruled out [8]. Understanding the mineralogy and morphology of Phobos goes a long way in assessing its viability as a waypoint for the human exploration of Mars.

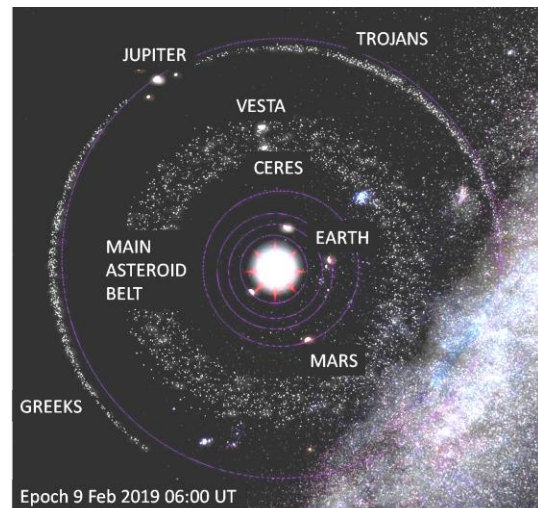


Figure 1: Inner solar system and asteroid populations

Some of the best resolution images of Phobos have been acquired by the High Resolution Imaging Science Experiment (HiRISE) camera on board the Mars Reconnaissance Orbiter (MRO). Figure 2 shows a composite picture acquired by HiRISE on 23 March,

2008 from a distance of 6800 km at a resolution of about 6.8 m/pixel [9]. The Mars Global Surveyor achieved a resolution of about 4 m/pixel. However, no spacecraft has ever carried out a sub-meter-scale survey of Phobos in the Visible/Near Infra-Red (VIS/NIR) and Short Wave Infra-Red (SWIR) spectral bands, information that is not only of scientific interest, but essential to identifying specific areas where resources may be mined during future human missions, and for identifying potential landing sites for robotic and human exploration.



Figure 2: Phobos from 6800 Kilometers as observed by the Mars Reconnaissance Orbiter HiRISE camera, 2008. Image credit: NASA/JPL-Caltech/University of Arizona

To this end, SHERPA’s strawman science / survey instruments used for spacecraft sizing consist of independent VIS/NIR (color) and SWIR (monochrome) cameras, with (commercially-available) sensor spectral responses as shown in Figure 3. The SWIR sensor is a 2D 9.5x7.6mm InGaAs thermo-electric cooled (-30°C) array with 15x15 μm cell size and broadband spectral range between 900 nm to 1700 nm. The VIS/NIR sensor is a 4.4x3.3mm Bayer RGB color CMOS array with 6.0 μm square pixels and spectral range between 390 nm to 1030 nm.

In addition to morphology and mineralogy, detection of water deposits on Phobos is highly desirable for In-Situ Resource Utilization (ISRU). The absorption spectrum of crystalline water ice has been shown to vary with temperature, with average peak positions from 20 to 240 K as shown in Figure 4 [10]. Of particular interest is the large peak with average position at 1.65 μm.

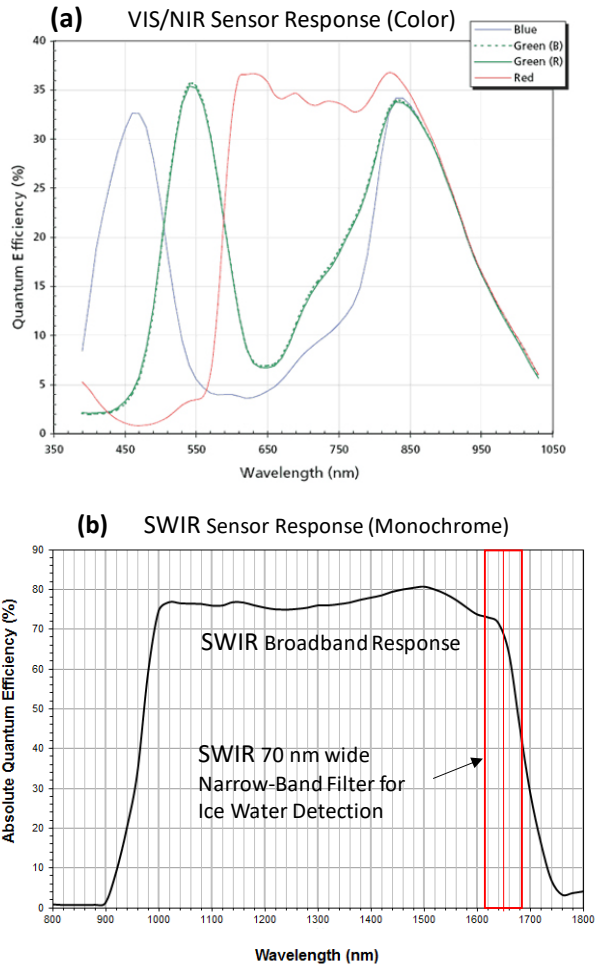


Figure 3: SHERPA strawman cameras spectral response (a) VIS/NIR color (b) SWIR Monochrome

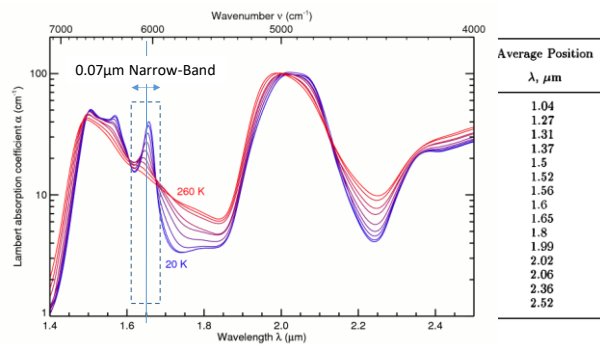


Figure 4: Water ice absorption spectra at SWIR with temperature average peaks (Grundy and Schmitt)

Derived single scattering albedo spectra (SSA) from CRISM onboard the Mars Reconnaissance Orbiter (MRO) is shown in Figure 5 [11]. Although the peak identified at ~1.68 μm is not addressed in the referenced

paper, it is possible that this feature has some water-bearing material. In order to focus on ice water detection, SHERPA includes a SWIR 70 nm-wide narrow-band filter with center frequency at 1650 nm. A flip-filter mechanism is included for alternate broad-band and narrow-band observations. The narrow-band chosen is highlighted in Figures 3b, 4 and 5, and range from 1615 to 1685 nm.

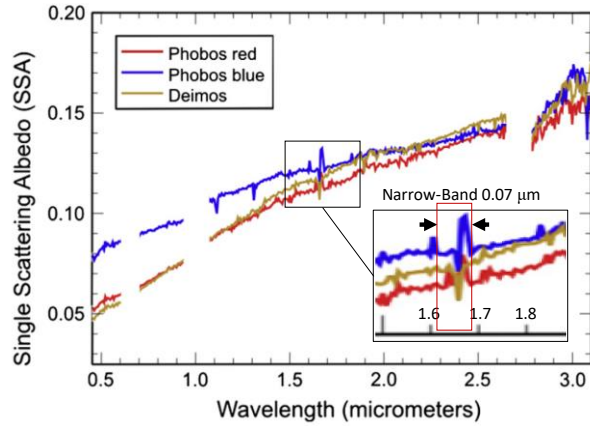


Figure 5: Derived single scattering albedo spectra showing possible water ice peak centered at $\sim 1.68 \mu\text{m}$ (Fraeman A. A., et. al.)

4. Instrument Payload

Phobos Survey Imagers

The strawman instruments used for spacecraft sizing consist of the aforementioned cameras, each paired to an $f/14$ 1250 mm focal length Maksutov-Cassegrain telescope. Assuming a 35 km nominal altitude DRO, the camera/telescope *spatial* resolutions are ~ 0.2 m/pixel for the VIS/NIR *color* camera, and ~ 0.4 m/pixel for the SWIR *monochrome* camera. Dropping the altitude to the minimum stable DRO orbit of 20 km, the resolutions increase to ~ 0.1 m/pixel (VIS/NIR) and ~ 0.3 m/pixel (SWIR). It is foreseen that such *spatial* resolutions coupled with spectral responses as shown in Figure 3 will lead to a wealth of information on Phobos mineralogy and morphology. Instruments used for hardware sizing are shown in Figure 5.



Figure 5: Strawman SHERPA imaging payload

Close Approach VIS Camera: Testing Regolith Cohesiveness

At the end of the mission, SHERPA will be commanded to approach Phobos enough to disturb its regolith with the spacecraft's main engine without actually touching down. A close-range imager is used to monitor the approach, and collect visual data of the encounter (as close as 10 meters depending on consumable status). This is a risky operation, and will require a methodical calibration of image size versus distance, and an accurate knowledge of Phobos gravity and "landing" location. The site can then be imaged to see the full effect of the plume impingement on the regolith, and to estimate its disturbed depth. This operation will consume about ~ 25 m/s starting from a 20 km DRO [5]. The camera is located in the aft section of the spacecraft, near the main engine. SHERPA's strawman close proximity imager is illustrated in Figure 6, shown on-board SMART. It is capable of imaging from ~ 10 m to infinity with minimal distortion.



Figure 6: Regolith impingement imager onboard SMART used for SHERPA's close proximity

Telecommunications Package

SHERPA has a 3 kg mass budget, and a 15/65 W nominal/peak power allocation for a Ka-Band transmitter unit operating at ~32 GHz. These allocations are in line with small satellite technologies already available. Figure 7 shows data rate estimates from Mars at conjunction (worst case) as a function of spacecraft High Gain Antenna (HGA) diameter, assuming use of the Deep Space Network's 70 m antenna. With parameters as shown in Table 1, the downlink rate point of inflection occurs at HGA diameters close to 1 meter. Hence, SHERPA's baseline 0.8 m diameter for the HGA results in a Shannon error-free rate limit of 21 kbps. If the DSN 34 m antenna is used instead, the worst-case rate drops to ~ 13 kbps. The mass/power allocation here is considered part of the spacecraft's payload.

The use of relatively high-speed transmissions for this class of vehicle points to the use of small satellites as viable data communications/relay satellites for scientific and human exploration. Since their replacement is much less costly than larger counterparts, demonstration of this function is highly desirable.

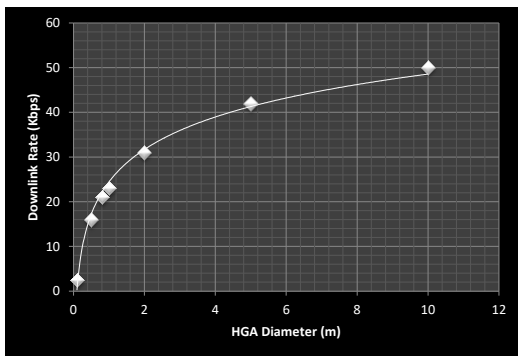


Figure 7: Downlink rate from Mars at opposition for different antenna diameters

Table 1: Link budget results for 0.8m HGA

RF Communications	Ka
RF Out (W)	6
HGA Dia. (m)	0.8
DSN Antenna (m)	70
DSN antenna efficiency	0.5
Total effective noise temperature (K)	68.5
Downlink Freq. (GHz)	32.3
SN receiver bandwidth (Hz)	4000
Slant Range (Km)	3.78E+08
Incidental Downlink losses (dB)	3
Effective Xmitter Antenna Area (m ²)	0.3
Effective Receiver antenna area (m ²)	1924
Xmitter Antenna Gain (dB)	46
Receiver Antenna Gain (dB)	84
Free space (or path) loss (dB)	294
SNR of Receiver (dB)	15
Transmit Rate - Shannon error-free limit (kbps)	21

5. Trajectory Design and ΔV Estimation

There are multiple examples of Mars mission designs that include injection into a Phobos DRO orbit. Since this study is focused on small-spacecraft as technology precursors for human exploration, the trajectory design was done in simple terms using Hohmann transfers, and only to constrain ΔV values used for the spacecraft sizing and mission analysis.

A Hohmann transfer to Mars results in a general trajectory as shown in Figure 8. No actual dates were used in this design, since this *minimum energy* approach could be applied to any given future Mars launch window. It is assumed the vehicle departs from a 185 km altitude circular Earth orbit, with a required C_3 of 8.7 km²/s² provided by the launch vehicle. Transit time to Mars is about 8.5 months, and the heliocentric arrival ΔV , or V-infinity of arrival is ~ 2.7 km/s.

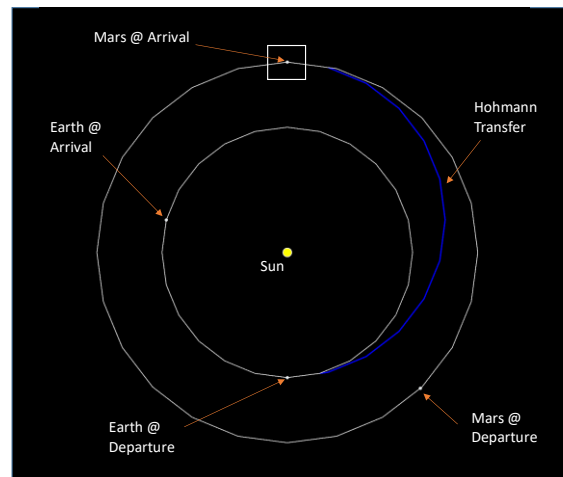


Figure 8: Hohmann transfer trajectory

The target altitude at Mars is 30 km, which is initially estimated geometrically to ensure enough atmosphere is encountered during aero-capture to effect a substantial insertion ΔV , without crashing to the surface (Figure 9). The spacecraft velocity at arrival, or entry speed is about 5.7 km/s. The entry interface is assumed to start at 195 km altitude.

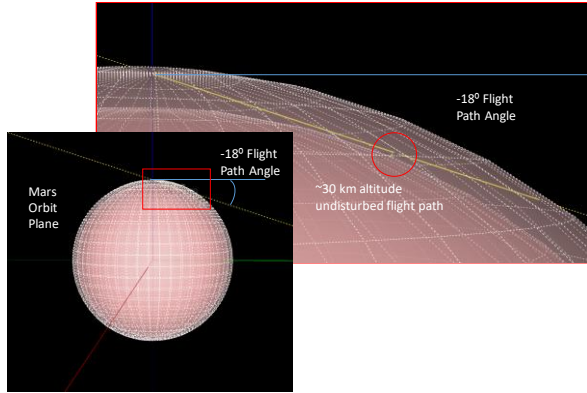


Figure 9: Geometric estimation of target altitude for Hohmann transfer arrival trajectory.

Past studies of Mars missions have assumed human-carrying spacecraft to start the landing maneuver at the apoapsis of a HMO one sol orbit 33800 km x 250 km above the mean Mars equatorial radius [5]. In order to gauge the Mars Orbit Insertion (MOI) ΔV required to achieve an initial orbit with varying apoapsis radii, we choose Phobos apoapsis radius (9517.58 km) as the starting minimum, and the reference elliptical apoapsis (33800 km) as the maximum radius. This also defines the ΔV to be effected by the aero-capture maneuver. Results are shown in Figure 10, with the minimum arrival orbit semi-major axis starting at 1.905 Mars radii, and the maximum at 5.012 Mars radii. The Phobos-to-HMO orbit ΔV ratio is about 1.5 (1.373 km/s \div 0.919 km/s), favoring the HMO orbit arrival. However, the larger 1.373 km/s ΔV is well within the bounds of aero-capture, so the realization of a Phobos-apoapsis orbit is essentially “fuel-free” (albeit not “mass-free”).

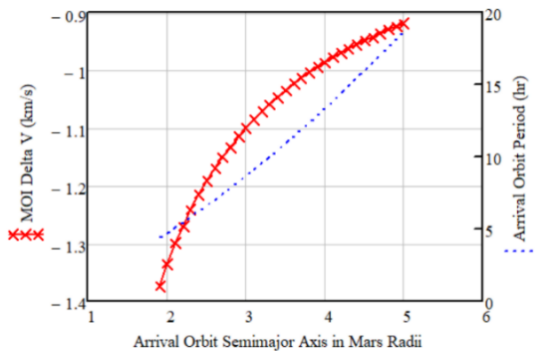


Figure 10: MOI ΔV requirements to achieve apoapsis radii from 9518 km to 33800 km, with periapsis at 30 km altitude.

Given the 1.373 km/s MOI ΔV provided by aero-capture, transfer maneuvers are then used to estimate the remaining ΔV s required to reach Phobos orbit. The first ΔV (797.7 m/s) is a combined in-plane and out-of-plane maneuver to an intermediate or “phasing” orbit to match

Phobos’ inclination (26.04° to the ecliptic), and raise periapsis out of Mars’ atmosphere (2030 km altitude). The second ΔV (297.4 m/s) is used to match Phobos orbit periapsis. The total ΔV required after aero-capture to match Phobos orbit is then ~ 1095 m/s. These maneuvers are illustrated in Figure 11.

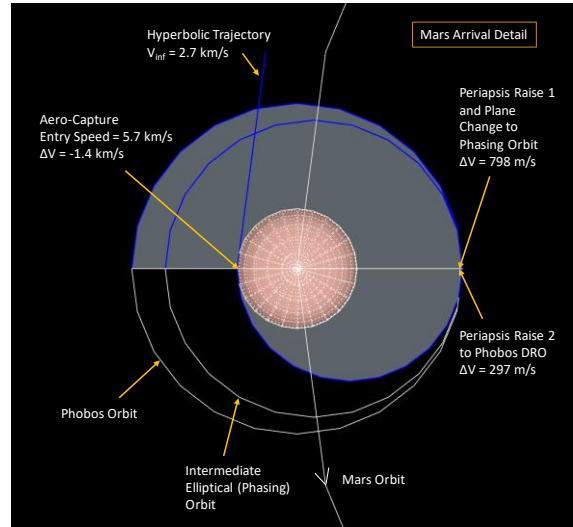


Figure 11: Transfer maneuvers to Phobos orbit defining ΔV requirements after aero-capture

Trajectory Correction Maneuvers (TCM) en route to Mars vary, but a good example to use is the Mars Reconnaissance Orbiter, totaling about 8.6 m/s [12]. We use 45 m/s of station-keeping and momentum wheel unloading for an operational life of 4 years, plus close proximity operations at end-of-life. Hence, the required total onboard ΔV is on the order of ~ 1149 m/s. This value was used to size the vehicle propulsion system using the rocket equation. Fuel margins will result from factoring a 30% contingency in the payload mass used for sizing the propulsion system, as will be seen. This ensures the vehicle is potentially able to remain at Phobos for many years beyond its 4-year baseline mission, providing several Mars synodic periods of Phobos science monitoring and telecommunications relay capability.

A detailed analysis of Phobos DRO orbits, their concept of operations, and maintenance ΔV can be found in the literature [13]. For the purpose of this example, we assume the “x-amplitude” is between 20 km and 35 km (must be above 20 and under 300 km for stability). The x-amplitude is defined as the largest distance from Phobos in the x-direction of a rotating frame of reference. It should be pointed out that the ΔV needed to maintain the final DRO orbit around Phobos is considered small for x-amplitude values larger than 20 km.

Although the orbit transfer maneuvers are simplified here, the analysis is sufficient to ascertain concept feasibility. Table 2 summarizes the trajectory and ΔV parameters.

Table 2: Earth-to-Mars Trajectory and ΔV requirements

Parameter	Value
Injection ΔV (Launch Vehicle)	3.6 km/s
C_3	8.7 km ² /s ²
Transfer Time	8.5 months
Mars arrival (entry) speed	5.7 km/s
Trajectory Correction Maneuvers	8.6 m/s
Mars Orbit Insertion (Aero-Capture ΔV) – To Phobos apoapsis	1.373 km/s
Periapsis raise maneuver 1 and Plane Change – to 2030 km altitude (Phasing Orbit)	797.7 m/s
Periapsis raise maneuver 2 – to Phobos periapsis radius	297.4 m/s
DRO Orbit Station Keeping, Momentum Unloading, and close approach operations	45 m/s

6. Spacecraft Sizing and Configuration

The trajectory design provides information needed to size the orbital vehicle propulsion system. This will not include the aero-capture system however, as the HIAD will be disposed of after aero-capture. It is important to recognize that the design process is inherently iterative. This paper presents the result of several iterations in relation to a definition of vehicle size and aerodynamic parameters, but it is by no means the “final” solution. For instance, the range of HIAD diameters used in this study was to be in-line with existing test articles built for testing by LaRC (between 3 to 6 meters)^[14]. The larger 6-meter diameter HIAD was the most promising choice *for this particular point design*, and was only selected after several iterations. As will be seen at the end of this paper, it is possible that a larger HIAD and/or new vehicle “packaging” behind the HIAD (e.g., stowed panels) may be needed to ameliorate potential harmful heating from super-heated airflow impinging on deployed solar panels. With that in mind, the vehicle/HIAD combination presented here represents a *feasible* implementation, with the caveat of impending iteration. Given the time and resource limitations constraining this study, that remains the subject of future work.

Propulsion System and Spacecraft Sizing

A blow-down hydrazine mono-propellant system with specific impulse $I_{sp} = 220$ s is used as the baseline for the propulsion system design. The propulsion system will be used for orbital maneuvering, en route for TCM, and to provide attitude control authority, with capability to provide continuous and pulsed operation. The initial vehicle mass is

$$m_{oc1} = m_{pc} + m_{tc} + m_{ec} + m_{Lc}$$

Where

m_{oc1} = Initial Vehicle Mass

m_{pc} = Propellant Mass

m_{tc} = Propellant Tank Mass

m_{ec} = Engine Mass (includes thruster structure, feed system, valves)

m_{Lc} = Payload Mass (Spacecraft minus the chemical propulsion system)

The payload mass (102.4 kg) corresponds to the spacecraft dry mass *except* propulsion system (tank, main engine, propellant) and HIAD, and includes a 30% contingency. Using the rocket equation, the initial vehicle mass is ~203 kg, and is given by

$$m_{oc1} := \frac{m_{Lc} + m_{ec}}{(1 + f_{tc}) \cdot \exp\left(\frac{-\Delta V_{CHEM}}{v_{e,CHEM}}\right) - f_{tc}}$$

Here $v_{e,CHEM}$ is the gaseous (~effective) exhaust velocity (2157 m/s), f_{tc} the tankage structure factor (0.2), and m_{ec} the engine mass (2 kg).

The propellant mass is ~84 kg, and is given by

$$m_{pc} := m_{oc1} \cdot \left(1 - \exp\left(\frac{-\Delta V_{CHEM}}{v_{e,CHEM}}\right)\right)$$

The tank mass (~17 kg) is obtained directly from the tankage structure factor

$$m_{tc} := f_{tc} \cdot m_{pc}$$

The main engine must be capable of executing trajectory corrections on the way to Mars, as well as orbit adjustments once there. In particular, the vehicle thrust / weight (F_{me}/W_s) ratio at Mars must be large enough to prevent excessive gravity losses from hindering the propulsion system's performance. To mitigate this effect, the F/W ratio should be in the order of 0.2 for space engines^[14]. Given this, and with a vehicle weight at Mars $W_s = 752.2$ N, the main engine thrust is 150.6 N,

$$F_{me} := FW \cdot W_s$$

Table 3 summarizes the vehicle mass and power sizing results, including propulsion system. It should be noted that the values shown in Table 2 are a combination of first principle calculations (e.g., rocket equation) and actual hardware (SMART bus).

Table 3: SHERPA Orbital vehicle sizing results

	Mass (kg)	Peak Power (w)
Orbiter		
Experiment Payload	9	71
Structure and Balance (incl. Solar Array)	25	
Thermal	4	26
Power and Harness	8	7
C&DH	2	22
RF Communications (DTE)	8	14
Guidance, Navigation and Control	5	39
Propulsion Module (excl. Tank and main engine)	16	22
Subtotal Dry	77.2	202
Contingency, 30%	23.2	60
Propellant	84	
Tank	17	
Main Engine	2	
Total Orbiter Wet	203	262
HIAD	186	
Total Launch Mass	389	
Falcon 9 (v1.0) capacity to C3 of 8.7 km ² /s ²	1417	
Solar Array Power (BOL)		633
Margin	264%	141%

Tables 4 and 5 show the battery and solar array sizing results.

Table 4: Li-Ion battery sizing results for 43-minute eclipse

Battery - Li-Ion	Value	Units
Load (incl. 30% Cont.)	82	Watts
Duration (1)	43	min
DOD	40	%
Battery Capacity	5	Ahr
Stored Energy	147	Whr
Mass	1.3	kg
(1) Eclipse at 250 km Altitude Circular Orbit		

Table 5: Solar array sizing results using flexible-type panels

UltraFlex Solar Array (TJ GaAsGe) - 1.5AU		
Load	262	Watts
Operating Life	4	years
Battery Charge	12	Watts
EOL Power	165	Watts
Off Nominal	30	Deg
Temp Degradation	0.00259	per DegC
BOL Power	633	Watts
Array Area	6	m ²
Solar Array Mass	9.9	kg
Specific Power (BOL)	63.8	W/kg

Spacecraft Configuration

Assuming a hydrazine density of 1.01 gm/cm³ and allowing for 3% ullage, the total tank volume is about 0.08 m³. Assuming a composite tank, its outer diameter is ~ 0.6 m. Aside from the spacecraft bus itself (existing design), the propulsion system tank and antenna sizes further constrain and define the vehicle overall dimension. The final result is shown in Figure 12 illustrating SHERPA in its deployed configuration.

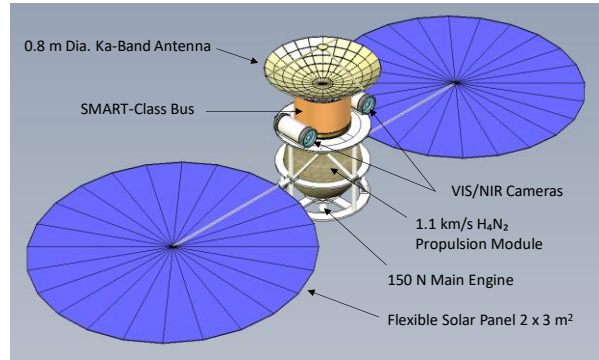


Figure 12: SHERPA with solar panels deployed

SHERPA's relative size is contextually illustrated in Figure 13, where it is shown in stowed configuration next to a ~1.8 m tall (5 feet 11 in) engineer. The packaged HIAD is not shown.

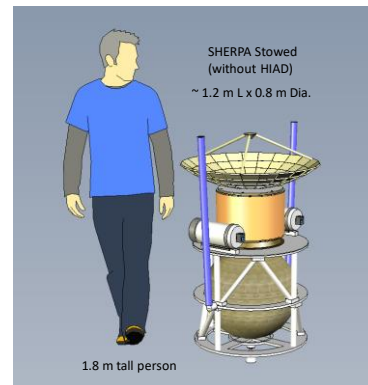


Figure 13: Illustrating SHERPA's relative size

Hypersonic Inflatable Aerodynamic Decelerator (HIAD) Design Assumptions

The conceptual HIAD for this study is based on one of LaRC's test articles with 6 m diameter. It is a sphere-cone design, with an estimated nose radius of 2.5 m and 70° half cone angle. The HIAD mass density is assumed to be ~40 kg/m³ deployed [16]. Given a material volume of ~ 4.65m³, its mass is estimated to be about 186 kg. Comparing this mass with a propulsive MOI option

yielding 1.373 km/s, the use of the HIAD results in a *net mass savings* of 196 kg, quite a significant number.

Several Computational Fluid Dynamics (CFD) simulations were carried out to find an optimal angle for the solar panel wings inside the HIAD. Results favor the panels feathered by 90° in order to lessen high-speed flow impingement on the vehicle. Figure 14 shows SHERPA accommodated in the HIAD, with its solar array wings stowed and ready for atmospheric flight. The simplified cross-section shows basic parameters defining the HIAD's geometry used in this analysis.

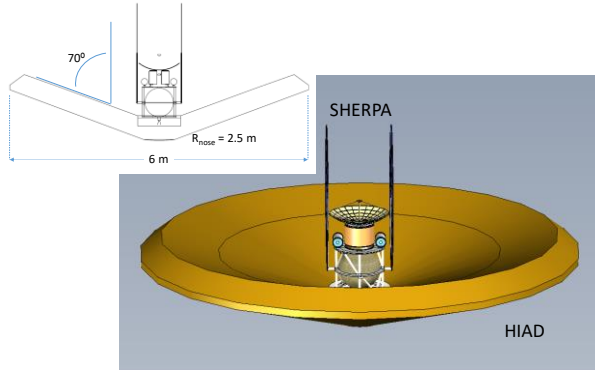


Figure 14: SHERPA inside 6 m diameter HIAD, wings feathered 90°, and ready for atmospheric flight

7. Aero-Capture Analysis

It was previously shown that the required aero-capture ΔV was 1.373 km/s. In order to ascertain feasibility, a simplified skip entry analysis is carried out, essentially a first order ballistic entry model with lift added [17]. The following assumptions are used:

- Zero-g, flat-Planet solution.
- Planar Trajectory.
- Non-rotating planet.
- Non-Thrusting entry.
- Entry Interface Conditions: r_e , V_e , ρ_e , and γ_e , corresponding to entry radius, velocity, density, and flight path angle, respectively.
- Entry density, $\rho_e = 0$.
- Model for atmospheric density $\rho_{mod}(h)$, is an exponential function of altitude (h).
- Vehicle control parameter: C_D (coefficient of Drag), C_L (coefficient of Lift).
- Small L/D or LD (Lift/Drag).
- Constant Scale Height, $1/\beta$.
- Constant ballistic coefficient ($m_{sn}/A_s C_D$), and L/D, where m_{sn} = vehicle mass, and A_s = vehicle reference area for lift and drag.

Simplified Exponential Atmospheric Model for Mars

A simple exponential density model is used for this analysis, and is given by

$$\rho_{mod}(h) := \rho_0 \cdot e^{-\beta \cdot h}$$

Here, h = height, ρ_0 = is the reference density (0.02 kg/m³), $1/\beta$ = scale height (8.3 km). The reference density is obtained from Mars-GRAM 2010 daytime data. The inverse scale height is 0.12 km⁻¹ and is derived from

$$\beta := \left(\frac{g_n}{R_{gas}} + T_{grad} \right) \cdot \frac{1}{T_{ref}}$$

Where g_n is Mars' surface gravity (3.71 m/s²), R_{gas} is the Martian gas constant (191.533 J/kg-K), T_{grad} is the temperature gradient (0.5 K/km), and T_{ref} is the reference temperature (165K). Both the reference temperature and gradient are estimated from Mars Pathfinder's altitude versus temperature curve, at the relevant altitudes for skip-entry (~30 to 195 km).

Skip-Entry Parameters

Symmetrical HIADs may have L/D up to 0.25 with movable Center of Gravity (CG) offsets [13]. For SHERPA, it is assumed that L/D ~ 0.24. The atmospheric *exit* velocity using this value is then given by

$$V_{ex} := V_e \cdot \exp\left(\frac{2 \cdot \gamma_e}{LD}\right)$$

Assuming L/D remains constant, the entry flight path angle is adjusted such that the exit velocity matches the periapsis velocity of an orbit with apoapsis at Phobos, as initially prescribed. In other words, the velocity $\Delta V = V_{ex} - V_e$ must equal -1.373 km/s, the aero-capture ΔV . By default, the entry flight path angle found this way does not match the initial undisturbed geometric estimate used for the interplanetary Hohmann transfer. The resulting flight path angle $\gamma_e = -1.91^\circ$ is consistent with the expectation that skip-entry analyses require small angles ($\sim < 5^\circ$). We must check that the calculated minimum altitude is above the Martian surface, or the vehicle will crash.

To that end we estimate the pull-up density (altitude) for the current conditions. After some iteration between this skip-entry analysis and CFD results, the coefficient of drag for SHERPA is set to $C_D = 1.44$. The vehicle

reference area for lift and drag is $A_s = 26.7 \text{ m}^2$. The vehicle mass was given as $m_{sn} = 389 \text{ kg}$, including the wet SHERPA *plus* the HIAD mass (Table 3). The spacecraft ballistic coefficient is then 10.1 kg/m^2 ,

$$C_B := \frac{m_{sn}}{A_s \cdot C_D}$$

The pull-up (or maximum) density is $5.64 \times 10^{-6} \text{ kg/m}^3$,

$$\rho_{max} := 2 \cdot \beta \cdot (1 - \cos(\gamma_e)) \cdot \frac{C_B}{LD}$$

Using the exponential atmospheric model, the corresponding minimum or pull-up altitude (67.9 km) is obtained by replacing ρ_{max} into

$$h(\rho) := \frac{-1}{\beta} \cdot \ln\left(\frac{\rho}{\rho_0}\right)$$

This result is well above Mars' surface.

The pressure drag force is roughly 21 times the vehicle weight at Mars, and is 30.52 kN. This is obtained from

$$F_d := C_D \cdot \frac{1}{2} \cdot 6.54 \cdot 10^{-5} \frac{\text{kg}}{\text{m}^3} \cdot V_{crit_skip}^2 \cdot A_s$$

Where the atmospheric density at ~50 km is used. Given this force, the deceleration is 78.4 m/s^2 ,

$$a_{df} := \frac{F_d}{m_{sn}}$$

In terms of Earth's gravity, the maximum vehicle deceleration is hence about 8 Gs, a manageable magnitude. Table 6 summarizes the basic aerodynamic parameters.

Table 6: Aerodynamic parameters

Parameter	Value
Ballistic Coefficient	10 kg/m ²
Lift/Drag	0.24
Pressure Drag Coefficient	1.44
Pressure Drag Force	30.5 kN
Deceleration	8 G
Pull-up Altitude	68 km

Atmospheric Heating Estimates

We now compute the entry heating parameters, both the *total entry heat load* as well as the *body average entry heating rate*. It is cautioned that the formulas used here have the skip-entry approximations built-in, and therefore the results are only order-of-magnitude estimates, useful for preliminary design. We assume that the primary source of energy input is convective heating from laminar boundary-layer flow over the entire vehicle. This is a reasonable approximation, since radiative heating is typically small for Mars entries as there are no strong radiators appearing in the chemical makeup of the dissociated gases^[18].

The Reynolds number for this case is 9216, and given by (dimensionless):

$$Re_L := \frac{\rho_{max} \cdot V_{ave} \cdot L_s}{\mu_{CO2}}$$

Where V_{ave} is the average entry/exit speed (4.97 km/s), μ_{CO2} is the dynamic (absolute) viscosity of CO₂ (the most abundant gas on Mars) at 165K ($8.2 \times 10^{-6} \text{ kg/m-s}$), and L_s is the vehicle reference length in the stream-wise direction (2.7 m). This value points toward a laminar flow pattern ($< \sim 500000$)^[19].

The body-averaged skin friction coefficient C_F (6.917×10^{-3}) is estimated from the Reynolds number using flat-plate theory, and is given by the equation

$$C_F := \frac{0.664}{\sqrt{Re_L}}$$

Flat-plate theory may be limited in these applications due to low-density reduction of the Reynolds number, which results in a boundary layer that may not be insignificant compared to the vehicle leading edge curvature. Nonetheless, CFD results show that although not insignificant, the boundary layer is still small compared to the vehicle body radius of curvature, and flat-plate theory can be marginally used in this case for preliminary analysis.

The *total heat load* (E_L) into the spacecraft is ~13 MJ, and is obtained from

$$E_L := \frac{1}{4} \cdot m_{sn} \cdot (V_e^2 - V_{ex}^2) \cdot \frac{S_w \cdot C_F}{A_s \cdot C_D}$$

Here, S_w is spacecraft body "wall" area exposed to entry heating, or *total aero-shell wetted area* (54.5 m²), which

in this case is the entire HIAD surface area. This equation is valid for an entry profile where the spacecraft slows-down sufficiently enough ("light" vehicle). The test is true by satisfying the following condition

$$0 < \dots -\sin(\gamma_e) = 0.033 < \dots \frac{1}{C_B} \cdot \frac{\rho_0}{\beta} = 16.417$$

It should be noted that the aero shell "wetted" area excludes SHERPA's orbital vehicle, as it is initially uncertain how much heat would be input onto it. Some insight will be gained from the CFD analysis shown later.

The *maximum body average heating rate*, and the density (altitude) and velocity at which it occurs are estimated from formulas applicable for *skip* entry. The maximum body average heating rate per unit area is about 17 W/cm² and is given by

$$q_{avmax_skip} := \frac{\beta}{4} \cdot C_B \cdot \gamma_e^2 \cdot V_e^3 \cdot \exp\left(\frac{3 \cdot \gamma_e}{LD}\right) \cdot \frac{1}{LD}$$

For comparison, the 3rd-generation HIAD technology development sought to improve the readiness level of the Flexible-TPS to ~ 75W/cm² @ 400°C [15], well beyond the range needed here.

The critical velocity at which maximum heating occurs is also the pull-up velocity, 4926 m/s is given by

$$V_{crit_skip} := V_e \cdot \exp\left(\frac{\gamma_e}{LD}\right)$$

Note this is about the average velocity between atmospheric entry and exit (4.97 km/s), which is what is expected at pull-up altitude.

Stagnation Point Heating

We compute the Stagnation Point heat flux for convection and radiation following equations given by Sutton and Graves [20], and Tauber and Sutton [21], respectively. Sutton-Graves simplified equation for *convective* heating at Mars results in 3.5 W/cm², and is given by

$$q_{spc} := k_m \cdot \sqrt{\frac{\rho_{max}}{R_{nose}}} \cdot V_{ave}^3$$

Where k_m is the Sutton-Graves constant for Mars (1.9027x10⁻⁴ m⁻¹ kg^{0.5}) as modified by Dec and Broun

[22], and R_{nose} , the sphere radius of the HIAD (~2.5 m). Note that the original Sutton-Graves tabular constant value was given for a mass fraction gas composition of 0.85 CO₂ and 0.15 N₂ and equaled 3.685x10⁻⁴ m⁻¹ kg^{0.5}.

Correspondingly, the *radiative* heat flux is 4.4x10⁻⁷ W/cm² given by

$$q_{spr} := C_r \cdot \left(\frac{R_{nose}}{m}\right)^{a_r} \cdot \left(\frac{\rho_{max}}{kg \cdot m^{-3}}\right)^{b_r} \cdot f_M$$

with constants as defined for Mars at a speed of 6 km/s, and in units of W/m². They are

$$C_r := 2.35 \cdot 10^4 \quad a_r := 0.526 \quad b_r := 1.19 \quad f_M := 0.2$$

The range of applicability of the radiative heat flux engineering correlation is close enough to its intended use, and hence suffices for preliminary analysis. It is also apparent that the radiative contribution for this case is insignificant compared to the convective counterpart, as had been previously assumed.

Radiation Adiabatic Wall Temperature

The maximum body temperature is estimated from the corresponding convective heat input at the stagnation point. If the entry vehicle surface is radiation cooled, and the heat flux into the wall has reached a state of nearly zero, then the wall temperature is in equilibrium and is equal to the radiation adiabatic temperature (a surface is called an "adiabatic surface" when no exchange of heat takes place). At this point, the wall temperature is the radiation adiabatic temperature. The actual emissivity of a material will vary depending on temperature and surface finish. We assume here that the HIAD has an emissivity of about 0.85, and use the (stagnation point) convective heating results. Given this, the heat balance ($q_{rad} = q_{conv}$) yields a wall temperature of about 923K (650° C), and is given by the equation

$$T_w := \sqrt[4]{\frac{q_{spc}}{\sigma \cdot \epsilon_s}}$$

This provides an estimate of the maximum wall temperature for a radiatively cooled surface. This temperature depends sharply on the TPS material properties. The value σ is the Stefan- Boltzmann constant (5.670400 x 10⁻⁸ W/m²-K⁴). Table 7 summarizes the entry heating results.

Table 7: Entry heating results based on skip-entry assumptions, and engineering correlations for stagnation point.

Parameter	Values
Reynolds Number	9216
Skin Friction Coefficient	6.917×10^{-3}
Total Heat Load	13 MJ
Max. Body Average Heating Rate	17 W/cm ²
Critical Velocity (@ $\gamma_e = 0$)	4926 m/s
Stagnation Point Heating – Convective	3.5 W/cm ²
Stagnation Point Heating – Radiative	4.4×10^{-7} W/cm ²
Radiation Adiabatic Wall Temp. @ Stagnation Point	923K (~650° C)

8. Vehicle Aerodynamics and CFD Analysis

In order to estimate the effects of atmospheric flight on the spacecraft within the HIAD, the system was analyzed using a CFD tool. The point in the trajectory chosen for the analysis corresponds to the maximum density, or pull-up altitude. However, a 26% margin was subtracted from the minimum altitude calculated in the skip-entry analysis, and the resulting 50 km altitude was then used for the analysis. Since the atmospheric density is greater at 50 km than 68 km, the aerodynamic effects will be more severe, and the results more conservative. Table 2 summarizes the boundary conditions used in the CFD analysis. Parameter values are derived from the 2010 Mars-GRAM during the day, and the results of the skip-entry analysis herein.

Table 2: CFD Parameter Input

Parameter	Values
Altitude above Mars	50 km
Density	6.54E-05 kg/m ³
Viscosity Coefficient @ 135K	6.61E-06 kg/m-s
Pressure	1.66 N/m ²
Mars Atmospheric Gas Constant	192 J/kg-K
Ratio of Specific Heats	1.3
Flow Speed	4926 m/s
Reference Area	26.7 m ²
Moment Reference Length	2.7 m
System Weight @ Mars	1444 N
Angle of Attack	0°

The velocity flow field is shown in Figure 15. As can be seen, the flow wraps around the HIAD front shell enough to impinge on the solar panels, and a flow pocket forms between the wings and the HIAD. Figure 16 shows a

surface map of the flow, indicating speeds as high at ~1500 m/s at some locations around the wing. The speed of sound at Mars’ relevant altitudes is 202.7 m/s, and is estimated by

$$c_s := \sqrt{\frac{\gamma_{CO2} \cdot R_u \cdot T_{ref}}{\mu}}$$

This means that the flow around the wing is supersonic at Mach ~ 7.

High-speed super-heated flow impinging on the solar panels will result in localized heating, as will be turbulent flow reflecting back onto the back side of the HIAD housing the spacecraft. From entry heating results, one would deduce that the localized average heating rate within a given wing area ~ 2.25 m² in size is about 380 kW (169 kW/m² x 2.25 m²).

Figure 17 shows the CFD steady-state radiation-boundary temperature solution scaled to the maximum radiation adiabatic wall temperature (923 K). This shows spacecraft surface temperatures ranging from about 7° C at the body of the bus to 192-283° C at the tip of the high-gain antenna and upper half of the solar panels. The front of the HIAD is mostly at ~ 428° C.

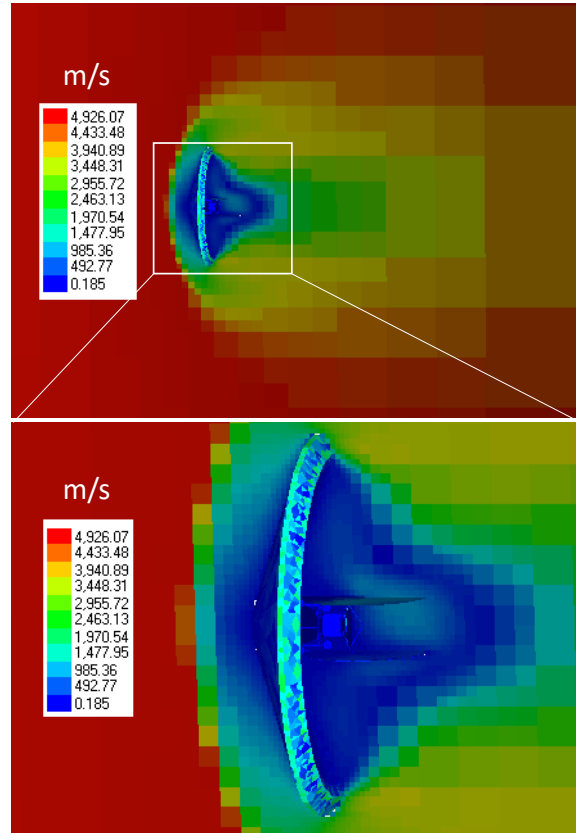


Figure 15: Velocity flow-field around SHERPA

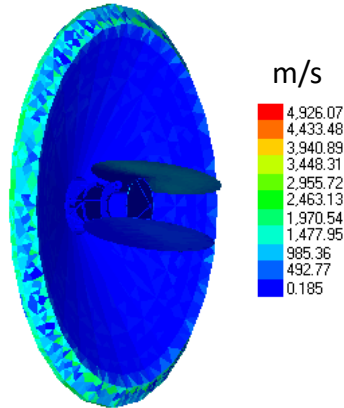


Figure 16: Surface flow on solar panels

These are results based on some conservative assumptions. The entire atmospheric flight (from 195 km to 195 km entry interface) lasts approximately 400 seconds through varying atmospheric densities and speeds; hence this is inherently a transient state analysis. Put in other terms, the vehicle will never reach steady-state, and is unlikely to see these extreme temperatures. Nonetheless, steady state “frames” provide a *worst-case* assessment of the expected thermal conditions, and help to point out locations where high temperatures are likely to occur. Mitigating measures may need to be taken to ensure materials are not exposed to temperatures that could cause structural damage. These may include a larger HIAD, or smaller spacecraft. The use of *CubeSats* may be a solution, with the tradeoff of less capability and shorter life expectancy than the current baseline. Nonetheless, the current design already shows preliminary *feasibility* as it stands.

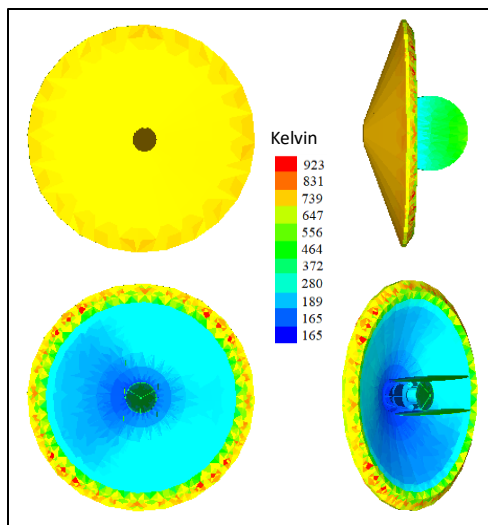


Figure 17: SHERPA surface temperatures at 50 km altitude scaled from stagnation point radiation adiabatic wall conditions

Notwithstanding the high flow around the solar wings for a limited period of time, the actual pressure is low given the rarified atmosphere encountered at Mars. This is illustrated in Figure 18, where the maximum pressure around the vehicle (including the wings) is a modest $\sim 138 \text{ N/m}^2$, or $\sim 0.0014 \text{ kgf/cm}^2$. With these results, it is clear that pressure loads are insignificant compared to aerodynamic heating. What does remain certain in any case is that we must endeavor to keep the entire spacecraft inside of the protective shadow of the HIAD as much as possible.

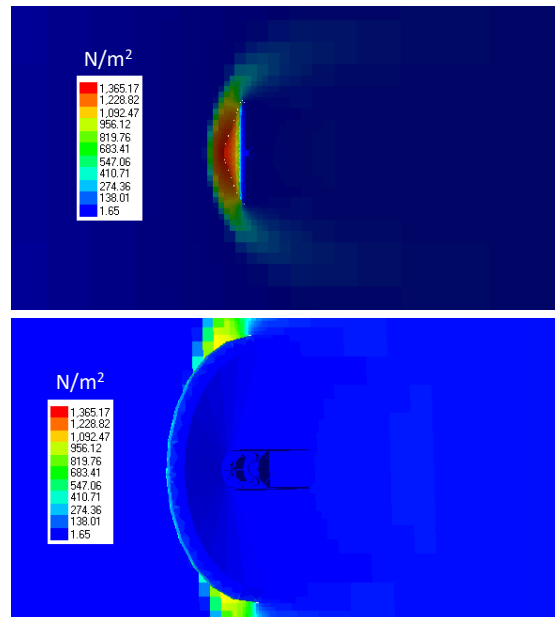


Figure 18: Pressure flow-field is small around SHERPA

9. Conclusions

An end-to-end mission was designed to provide context on which to analyze the feasibility of using small satellites together with aero-capture technology in order to carry out scientific exploration of Phobos ahead of human arrival. We believe the results successfully advocate for the use of small satellites to carry out scientific exploration of the Mars system, and to test out technologies and operational concepts needed in the sustained human exploration of Mars. Consistent with a systems engineering approach, this work described a *feasible* scenario for science acquisition, technology verification, trajectory validation, and in-situ resource exploration that bridges all NASA Directorates. Ascertaining mission feasibility with the relatively modest resources available to small satellites and CubeSats help to further their application as trailblazers in human and robotic exploration.

10. Acknowledgements

The authors wish to thank the following individuals for reviewing the concept/paper and providing insightful feedback: Conor Nixon, Scott Guzewich and David Everett (NASA Goddard Space Flight Center), Michelle Rucker and John Connolly (NASA Johnson Space Center).

11. References

1. Aldrin, Buzz, L. David, "Mission to Mars: My Vision for Space Exploration," National Geographic Books, 2013.
2. Esper, J., "Modular, Adaptive, Reconfigurable Systems: Technology for Sustainable, Reliable, Effective, and Affordable Space Exploration," Proceedings of the Space Technology and Applications International Forum, American Institute of Physics, 2005. Taylor & Francis, London/ Leiden/ New York/ Philadelphia/ Singapore.
3. Esper, J., "Small Rocket/Spacecraft Technology (SMART) Platform", Small Satellite Conference, Logan Utah, August 2011.
4. National Academy Space Studies Board, "Visions and Voyages for Planetary Science in the Decade 2013 – 2022," March 7, 2011.
5. Cianciolo, Alicia D., Kendall Brown, "Impact of Utilizing Phobos and Deimos as Waypoints for Mars Human Surface Missions," AIAA SPACE Conference and Exposition, 2014
6. Abercromby, Andrew F. J., *et. al.*, "Human Exploration of Phobos," IEEE Aerospace Conference, Big Sky, Montana, 2015
7. Murchie Scott L., *et. al.*, "The Scientific Rationale for Robotic Exploration of Phobos and Deimos," Whitepaper, 2009.
8. Fanale, Fraser P., James R. Salvail, "Loss of water from Phobos". Geophysical Research Letters (ISSN 0094-8276), vol. 16, April 1989, p. 287-290.
9. <https://hirise.lpl.arizona.edu/phobos.php>
10. Grundy, W.M., and B. Schmitt, "The Temperature-Dependent Near-Infrared Absorption Spectrum of Hexagonal H₂O Ice," J. Geophys. Res. 103, 25,809-25,822, 1998.
11. Fraeman A. A., *et. al.*, "Spectral absorptions on Phobos and Deimos in the visible/near infrared wavelengths and their compositional constraints" Icarus 229 (2014) 196–205.
12. You, Tung-Han, *et. al.*, "Mars Reconnaissance Orbiter Interplanetary Cruise Navigation", 20th International Symposium on Space Flight Dynamics, Annapolis MD 2007.
13. Conte, Davide, David B. Spencer, "Mission analysis for Earth to Mars-Phobos distant Retrograde Orbits", Acta Astronautica 151 (2018) 761–771.
14. Johnson, R. Keith. *et. al.*, "HIAD Advancements and Extension of Mission Applications", IPPW-13, Laurel, MD 2016.
15. Humble, R.W., G. H. Henry, and W. J. Larson, ed.: "Space Propulsion Analysis and Design," McGraw Hill, Inc., New York, 1995.
16. Del Corso, Joseph A. *et. al.*, "Hypersonic Inflatable Aerodynamic Decelerator Ground Test Development", IPPW-12, San Jose, CA 2015.
17. Griffin, M. D., and J. R. French: "Space Vehicle Design," American Institute of Aeronautics and Astronautics, Washington, D.C., 1991.
18. Wright, Henry S. *et. al.*, "Mars Aerocapture Systems Study," NASA/TM-2006-214522, 2006.
19. Bertin, John J., Michael L. Smith, "Aerodynamics for Engineers," Second Edition, Prentice Hall Inc., 1989.
20. Sutton, K., and R. A. Graves A., "General Stagnation-Point Convective-Heating Equation for Arbitrary Gas Mixtures," NASA TR R-376, 1971.
21. Tauber, M. E., K. Sutton, "Stagnation-Point Radiative Heating Relations for Earth and Mars Entries", Journal of Spacecraft and Rockets, Vol. 28, No 1, 1991, pp.40-42.
22. Dec, John A., R. D. Broun, "An Approximate Ablative Thermal Protection System Sizing Tool for Entry System Design," 44th AIAA Aerospace Sciences Meeting and Exhibit, Aerospace Sciences Meetings, Reno, Nevada 2006.